Ultrafast nonlinear control of progressively loaded, single plasmonic nanoantennas fabricated using helium ion milling

Yudong Wang,[†,‡] Martina Abb,[†] Stuart A. Boden,[‡] Javier Aizpurua,[¶] C. H. de Groot,[‡] and Otto L. Muskens[*,†]

Physics & Astronomy, Faculty of Physical Sciences and Engineering, University of Southampton, Highfield, Southampton SO17 1BJ, United Kingdom, Nano Group, Faculty of Physical Sciences and Engineering, University of Southampton, Highfield, Southampton SO17 1BJ, United Kingdom, and Donostia International Physics Center, DIPC, and Centro de Fisica de Materiales CSIC-UPV/EHU, Paseo Manuel Lardizabal 4, Donostia-San Sebastian 20018, Spain

E-mail: O.Muskens@soton.ac.uk

Abstract

We demonstrate milling of partial antenna gaps and narrow conducting bridges with nanometer precision using a helium ion beam microscope. Single particle spectroscopy shows large shifts in the plasmonic mode spectrum of the milled antennas, associated with the transition from capacitive to conductive gap loading. A conducting bridge of nanometer height is found sufficient to shift the antenna from the capacitive to the

[*]To whom correspondence should be addressed
[†]Physics & Astronomy, University of Southampton
[‡]Nano Group, University of Southampton
[¶]DIPC and CSIC-UPV/EHU

conductive coupling regime, in agreement with circuit theory. Picosecond pump-probe spectroscopy reveals an enhanced nonlinear response for partially milled antennas, reaching an optimum value for an intermediate bridge height. Our results show that manipulation of the antenna load can be used to increase the nonlinear response of plasmonic antennas.

Keywords: nanoantenna; nonlinear plasmonics; helium ion; conductive coupling; Fano resonance

Plasmonic nanoantennas are of interest for their capacity of controlling light on the nanoscale.[1] In particular, precise control of plasmonic near-field interactions on (sub-)nanometer length scales is of interest for achieving strongly enhanced local fields as well as for exploring the fundamental limits of nonlocal and quantum plasmonic effects.[2–4] Such applications require pushing the limits of nanofabrication to new levels of precision and control. Electron beam lithography (EBL) is a well established tool capable of obtaining very small nanogaps between nanoparticles.[5] The limitations of resists and undercuts however pose constraints to the type of structures and nanogaps that can be obtained. Complementary methods such as electrochemical deposition can be used to achieve even smaller features down to the sub-nanometer range.[6,7]

Patterning of substrates using focused ion beams is a versatile method for obtaining a variety of plasmonic and metamaterial devices. Focused ion beam (FIB) milling has been successfully applied to the fabrication of partial nanogaps, where part of the material in the gap was removed from the sides to obtain a thin conducting bridge of controlled dimensions.[8,9] Compared to FIB milling which uses relatively heavy Ga ions, new opportunities emerge with the increasing availability of other sources of lighter elements such as helium. The helium ion microscope is a surface imaging tool which scans a helium ion beam across a surface to form an image. It is similar to a scanning electron microscope (SEM), but due to the larger mass and therefore smaller de Broglie wavelength of a helium ion, combined with

its atomic scale source, it is able to produce a smaller probe size compared to an advanced SEM. This leads to a small interaction volume and therefore high resolution imaging.[10] The helium ion microscope is also a patterning tool which can be used to pattern resist like EBL[11] or can be used for direct writing on the substrate like a FIB.[12] Helium ion milling (HIM) has been applied successfully to the structuring of a variety of systems such as silicon nitride,[12] graphene[13] and magnetic spin valves.[14] Recently, the first plasmonic application was reported where HIM was used to obtain narrow (< 5 nm) plasmonic resonators in a crystalline Au substrate.[15]

Here, we demonstrate the use of helium ion milling in the fabrication of plasmonic nanoantennas with partially loaded nanogaps. We make use of the fact that HIM is a relatively gentle method which removes material from the top surface in a layer by layer fashion.[14] Compared to FIB milling, much more control over the precise nanoscale morphology of the nanogap is possible using the helium ion technology. By incremental milling, it is therefore possible to obtain precise control over the height of individual nanometer-scale areas. We use this property to obtain vertically milled partial gaps, which cannot be obtained easily using other methods. The optical response of the HIM milled antennas is subsequently characterized using single-particle linear and pump-probe spectroscopy. In particular, we are interested in analyzing the potential of partially conductive gaps to provide an enhanced sensitivity to nonlinearity and/or to changes in the local environment.

Nanoantennas were fabricated on a Borofloat 33 glass substrate using electron beam lithography (JEOL 9300FS) and liftoff. The process firstly involved spinning a copolymer (MMA) layer on the substrate to a thickness of 250 nm followed by a polymethylmethacrylate (PMMA) layer on top to a thickness of 150 nm. A 20 nm thick conducting copolymer layer (Espacer 300Z) was used to prevent charging during electron beam exposure. EBL was carried out at an accelerating voltage of 100kV and an exposure current of 1 nA to deliver a dose of 600 μC/cm^2. Dose optimization and proximity effect correction were carried out as described in previous work.[16] After exposure the resist was developed in methyl isobutyl

ketone (MIBK) : isopropyl alcohol (IPA) 1 : 1 for 60 s. A 2 nm-thick Ti adhesive layer and 30 nm-thick Au were evaporated in Leybold Optics LAB700eb evaporator at a pressure of 5×10^{-6} mBar. The lift-off was done manually by soaking in N-Methyl-2-pyrrolidone (NMP) for 20 mins.

Helium ion beam milling was carried out with a Carl Zeiss OrionPLUS^{TM} helium ion beam microscope. The sample was cleaned by soaking in NMP at room temperature followed by IPA rinsing to remove any organic residues. This is an important step because hydrocarbon contamination of such materials leads to helium ion beam assisted deposition on any surfaces where the beam scans. The line-shaped gap of the dimer was defined in binary bitmap format, with one pixel corresponding to 1 nm, which was imported by the Orion software to enable the patterning function. The alignment of the pattern was based on an image of the nanoantenna taken by the helium ion microscope before milling. The milling conditions were chosen as 1 pA current, 10 μm aperture size, 10 μs dwell time, leading to a base dose of 6.154 $\times 10^{15}$ ions/cm^2. The milling current was optimized by considering the total substrate drift during the milling and the amount of He implanted into the substrate when taking the alignment image. Multiple scans were used to deliver the required total dose for milling completely through the Au layer. The required total dose was first estimated by Monte Carlo modeling and then optimized experimentally using SEM inspection and resistance measurements as described further below. The ion milling process was simulated by the SRIM software package.[17] The simulation modeled the 30 keV He ions sputtered onto a multilayer of 30 nm thick Au, 2 nm Ti and a SiO_2 substrate. For 100,000 ions the average milling rate was calculated to be 0.124 atoms/ion.

In our experiments, antennas were milled either from the sides or from the top as illustrated in Figure 1a. While the amount of milling from the sides could be precisely characterized using SEM, standard techniques such as atomic force microscopy or SEM cannot provide reliable depth information for the narrow, high aspect ratio nanogaps. In order to calibrate the depth of nanogaps obtained using HIM from the top, we performed electrical

resistance measurements using a calibration sample. Partially milled gaps were fabricated in electrically contacted gold lines of the same lateral dimensions as the nanoantennas (i.e. 30 nm height, 80 nm width). A four-point measurement setup allowed probing of the resistance of the nanogap, independent of the resistance of the whole measurement system. The fabrication of such a four-point resistance measurement system can be found in previous work.[18] The starting point of the milling experiment was selected around the calculated milling dose between 100 and 600 times the base dose. The resistance of each Au wire was measured before and after the milling. The change of conductance of the milled area is proportional to the milling depth. Partial gaps of widths as small as 5 nm could be obtained by varying the milling width of the focused helium ion beam, as shown in Figure 1b. Values for the bridge height, obtained from the wire conductance, are shown in Figure 1c versus the number of repeats of the base dose milling for milling widths of 20 nm, 10 nm and 5 nm. It was found that milling widths of 20 nm, 10 nm and 5 nm resulted in milling rates of respectively 0.064 atoms/ion 0.050 atoms/ion and 0.038 atoms/ion [Figure 1d]. The drop in milling efficiency with decreasing milling width is attributed to the increase of side wall resputtering. At the milling width of 20 nm, the milling efficiency of 0.064 atoms/ion is about half of the simulated value of 0.124 atoms/ion which agrees with earlier results found for Ni.[14] For both the calibration sample and the nanonantennas, it was found that the edge of the structure was milled through faster than the center, resulting in a reduced bridge width even for homogeneous milling from the top. We attribute this to the fact that the metal lines are slightly thicker in the center, as observed by atomic force microscopy (see Supplementary Information). For simplicity of analysis, we use in the following an effective bridge height assuming a constant bridge width, which is representative of the geometrical cross section of the remaining electrical contact.

Extinction spectra of individual nanoantennas were measured using the method of Spatial Modulation Microscopy (SMM).[19–21] In short, SMM is based on the periodic modulation of a nanoparticle in a tightly focused beam. The amount of transmitted and reflected light

depends on the position of the nanoparticle in the beam profile, which can be demodulated with high sensitivity using lock-in detection. Compared to earlier work,[22,23] the setup was extended to cover the near-infrared range. The output of a broadband supercontinuum light source (Fianium, 450 nm - 2500 nm) was filtered to a spectral band of several nm using a subtractive mode prism monochromator. The light was focused onto a single nanoantenna by means of a reflective Cassegrain objective (Edmund Optics, 0.5 N.A.). Reflected light from the sample was spatially filtered using a confocal pinhole and was detected using an InGaAs photodiode (Thorlabs). A piezo-actuated flexure mirror produced a periodic displacement of the focus with an amplitude of 1.3 μm at a modulation frequency of 200 Hz. A dual-reference lock-in amplifier (Ametek) was used to simultaneously demodulate the SMM modulation signal ΔR and the reflected intensity R (modulated using a chopper). We used the second harmonic of the electronic SMM signal to obtain a relative differential signal $\Delta R/R$ which was maximum when the antenna was positioned at the center of the beam focus for all wavelengths.[19,20] The $\Delta R/R$ signal is directly proportional to the extinction cross section σ and can be used to retrieve the absolute extinction spectra of the nanoantenna. In analogy with Ref.,[21] we write for a Gaussian beam profile $I(x) \sim \exp(-x^2/\rho^2)$ the relation as

$$\sigma = \frac{\pi\rho^2}{\xi_{2f} R_{\text{subs}}} \frac{\Delta R}{R}|_{x=0} \tag{1}$$

Here ρ is the $1/e$ beam waist, ξ_{2f} relates the relative differential signal $\Delta R/R$ at the particle position ($x = 0$) to the modulation amplitude δ. For small modulation amplitudes $\delta << \rho$ the function scales as $\xi_{2f} \simeq \delta^2/\rho^2$, while for $\delta/\rho \sim 1$, it flattens off to a value of $\xi_{2f} \simeq 0.5$. Therefore, in the range of our experiment, ξ_{2f} depends only weakly on wavelength. After calibration of the beam width ρ and substrate reflectivity R_{subs}, eq 1 was used to obtain the experimental extinction cross-section of the nanoantennas.

Figure 2 shows the experimental extinction cross sections σ obtained for antennas of total length $L = 620$ nm under different milling conditions. Nanoantennas A-G were completely milled through from the sides with a milling width of 20 nm, leaving a bridge of variable width

in the center of the gap. Nanoantennas H-N were milled from the top using a constant number of 400 repeats, while the milling width was varied from 5 to 20 nm. The average height of the connecting bridge was estimated using the milling dose calibration from Figure 1. This method resulted in good control over the conducting bridge in the critical regime. Results for several other milling conditions are shown in the Supplementary Information.

The unmilled antennas (A, H) show extinction resonances at 1100 nm and around 2500 nm which correspond well with the expected $3\lambda/2$ and $\lambda/2$ modes of a single 620 nm nanorod. Respective milling from the sides (from A to G) or from the top (from H to N) results in a redshift of the antenna modes. This phenomenon can be explained by the transition from an conductively to a capacitively loaded antenna gap,[8,24] as will be discussed below. For completely milled gaps (G,N), we find a mode at a wavelength of 2000 nm corresponding to the capacitively coupled $\lambda/2$ resonances of the individual antenna arms.

For several of the conductively coupled antennas A-D and H-L, the $3\lambda/2$ mode shows an asymmetric profile with a steep edge at the long wavelength side. This feature is illustrated for antenna A by the arrow at 1200 nm wavelength. Recent theoretical predictions have attributed this characteristic feature to a Fano interference between the resonant scattered field from the higher-order $3\lambda/2$ mode with a flat background corresponding to the tail of the fundamental resonance of the same antenna.[25] The estimated background level is illustrated by the dashed line in the spectrum of A. The Fano interference between different modes of a single antenna is of interest for applications in sensing.[26] This feature will also be important in the interpretation of the nonlinear response further below.

Figure 3a and b show the experimentally obtained resonance positions for the antennas of Figure 2 (diamonds, blue); for each milling configuration a second series was obtained as indicated by the red dots, showing the robustness of the milling process (see Supplementary Information). Lines in Figure 3 correspond to estimated resonance positions using circuit theory. We used standard antenna theory[27] corrected by an effective wavelength scaling of the antenna length at optical frequencies.[28] Following the approach of Schnell et al.,[8]

the scattering resonances of an unfed antenna for a plane wave incident light field can be modeled as a series combination of the impedances of the dipole antenna Z_{dip} and the gap load Z_{load}. The bridge and gap impedances are approximated as $Z_{\mathrm{bridge}} = g/i\omega\epsilon_{\mathrm{Au}}hw$ and $Z_{\mathrm{gap}} = g/i\omega\epsilon_{\mathrm{eff}}(h_0w_0 - hw)$,[29] where h_0 and w_0 are the height and width of the antennas and h, w the dimensions of the bridge. Furthermore g denotes the gap width and $\omega = 2\pi c/\lambda$ the angular frequency of light. The load impedance $Z_{\mathrm{load}} = R_{\mathrm{load}} - iX_{\mathrm{load}}$ is then obtained through the parallel addition of Z_{bridge} and Z_{gap}.

The spectral resonance positions of the loaded antenna follow from the condition where the reactance X_{dip} of the dipole is matched by that of the load, $X_{\mathrm{dip}} + X_{\mathrm{load}} = 0$. We use antenna circuit theory to describe the reactance of the flat dipole antenna as that corresponding to an effective cylindrical dipole antenna of radius a=0.25w, and same length L [Ref.[27]]. A detailed explanation of this method is given in the Supplementary Information. The solution to the reactance matching for different bridge dimensions are indicated by the lines in Figure 3a and b. The dashed black line corresponds to the critical condition where X_{load} crosses over from capacitive to inductive behavior. The red line on the left of the critical condition corresponds to the fundamental bonding mode of the capacitively loaded antenna, while the green lines represent the $\lambda/2$ and $3\lambda/2$ bonding modes of the inductively loaded antenna. These solutions are separated by a gap where no modes are found. In our model, the effective antenna length was optimized to achieve good agreement with the modes of the inductively loaded antenna. The capacitive coupling was subsequently adjusted to obtain agreement with the measured resonance for the fully milled antennas, yielding a capacitance of 10.2 aF. Both experiments and model show an scaling of the critical size with width and height proportional to the total area fraction $h \times w$ of the metallic bridge, as expected for the simple approximation of the gap as a parallel composition of a capacitive and an inductive impedance proportional to the area of the elements. Furthermore, for vertically milled antennas, the model predicts a critical transition for only a few nm thickness, in agreement with experiments which show the largest shifts for this range. Our experimental results for

these narrow bridges however do not allow a detailed quantitative comparison with theory as small variations from antenna to antenna may affect the precise resonance position in this range. We note that similar sensitive tuning of antenna modes has recently been obtained using a thin film metal substrate,[30] consistent with our findings.

While the circuit theory provides the spectral positions of antenna resonances, it does not give quantitative information on the shape and amplitude of the spectrum. Therefore, we performed numerical finite-element calculations of conductively loaded antennas for the experimental geometries under study. The antenna parameters were fixed to the measured dimensions of $L \times w_0 \times h_0 = 300 \times 80 \times 30$ nm^3 for the individual arms. The antenna gap was incrementally loaded by an Au bridge. Figure 4 a and b show the resulting spectra, with peak positions plotted in Figure 4 c and d (diamonds, black). The dashed spectra in Figure 4 a and b represents two times the cross-section of a single arm nanoantenna with the above dimensions, corresponding to the case without any capacitive or conductive coupling. While the capacitively loaded antenna (orange curve) starts with a redshift compared to the uncoupled case, a cross over to a blueshifted resonance is obtained for less than 1 nm bridge height or 5 nm bridge width. The resonance wavelength versus bridge size shows a smooth transition between the fundamental resonance of the capacitive antenna to the higher order mode of the conductively coupled antenna, without a clear gap in the cross over as given by antenna theory (Figure 3). This behavior is similar to numerical and experimental results found in other work.[8,9] The presence of the gap is natural as the circuit theory does not support solutions which are at the same time capacitive and inductive; the impedance load diverges and one mode dies out before the other sets in. Numerical calculations capture the gradual transition, as is shown by the near-field maps of Figure 4e.

Figure 4e illustrates the evolution of the antenna mode from a full-length $3\lambda/2$ resonance as the bridge height is reduced from bottom to top. The gradual transition to two $\lambda/2$ coupled dipoles for $h = 0$ involves converting the π phase angle shift over the antenna length into a phase jump of the field at the gap, as was investigated into detail in Ref.[8] Compared

to the spectral resonance shift, the maximum electric field enhancement in the gap (red dots in Figure 4d) shows a much less steep dependence for small bridge height. Conductive gap loading using a nanometer scale vertical bridge may thus provide a sensitive method for tuning the resonance wavelength without strongly affecting the local near-field enhancement or changing the overall antenna length.

The likely presence of the Fano profile in the linear spectra can be tested by comparing the resonances with a Lorentz oscillator model (see Supporting Information). This analysis shows a small contribution of the Fano resonance in the particular structure under study. Comparison of the Fano resonances of different antenna geometries found a much smaller effect for rectangular shaped antennas than, for example, for spheroidal nanoparticles.[25] Compared to the linear spectra, the Fano interference presents itself more clearly in the nonlinear antenna response, as will be shown below.

The large resonance shift with only a very small amount of material is of potential interest for applications in optical sensing or nonlinear control. Here, we investigate the nonlinear response of the vertically milled antennas induced by picosecond pulsed laser excitation. Picosecond pump-probe experiments were conducted by using the supercontinuum light source as a probe, while the frequency doubled secondary output of the same oscillator was used as a pump to excite the nanoantennas at 530 nm wavelength[22,23] (see Figure 5a).

Figure 5a and b show typical results for antenna J in Figure 2 for the pump-probe change $\Delta\sigma$, normalized to the maximum $\sigma_{\max}$ of the resonance. The red line in the lower panel of Figure 5a corresponds to the ultrafast modulation after subtraction of a stationary heat background (black line). The dynamics of the nonlinear modulation are plotted as a function of wavelength and pump-probe delay time in Figure 5b. The picosecond dynamics are consistent with the expected behavior for pulsed excitation of the Au antenna,[23,31] where the decay time of several hundred ps corresponds to cooling down of the antenna through phonon transport. Our ps laser does not allow resolving the fast, sub-ps dynamics corresponding to hot electron effects.

The picosecond nonlinear modulation was measured for a number of antennas milled from the top, i.e. with different bridge heights, yielding the nonlinear response $\Delta\sigma/\sigma_{\max}$ as shown in Figure 5. We note that as some of the antennas were damaged in the pump-probe experiment, we combined the series H-M from Figure 2 with antenna X from the Supporting Information. The maximum nonlinear signal follows the spectral shift of the antenna modes. We note that, next to a strong negative contribution which can be attributed to plasmon bleaching, a positive peak is observed for some of the antennas on the long wavelength side of the resonance. This second peak exceeds the small positive wings on both sides of the resonances expected for plasmon bleaching. In fact, the positive peak is a nonlinear signature from the Fano profile of the higher order antenna mode as discussed in Figure 2. As the Fano dip in the linear spectrum corresponds to a destructive interference of the resonant mode with the nonresonant background, the bleaching of the resonant contribution results in an reduced interference and thus a positive differential pump-probe signal. Good agreement is obtained for the nonlinear response with our finite element calculations shown in Figure 5d. Here, the nonlinearity is modeled as a 20% change in the Drude damping time, τ_D. The change in damping results in a nonlinear coefficient which is mostly imaginary (see Supplementary Information), in agreement with other pump-probe studies of Au nanorods in the near infrared.[22,31]

The nonlinear signals in Figure 5d correspond to the calculated cross sections of Figure 4b and show a shift with resonance position. Both experimental and calculated nonlinear spectra show a marked increase of $\Delta\sigma/\sigma_{\max}$ for an intermediate range of antenna gaps of around 5 nm. This optimum thickness shows an effect of the bridge height on the nonlinear response, which cannot be explained by variations in the bulk nonlinear coefficient as shown in the Supplementary Information. The purely imaginary nonlinearity can be associated to a modulation of the load resistance. The increased resistive load results in an additional damping of the antenna mode, which adds to the damping of the dipole antenna resonance by the dielectric nonlinearity. The resistive load initially increases with bridge height, however it

saturates when the conductive bridge is formed. This behavior is consistent with the spectral narrowing of the resonance line as the mode evolves from a fundamental dipole to a higher-order antenna resonance. The spectral narrowing is associated with an increased dwell time, and thus a stronger susceptibility to the nonlinear load resistance. The reduction of the nonlinear signal $\Delta\sigma/\sigma_{\max}$ for larger bridge heights can be explained by the strong reduction of the resonant mode cross section compared to the nonresonant background (see Figure 4b). Thus the nonresonant part of $\sigma_{\max}$ reduces the relative strength of the resonant nonlinear response. While the current work investigated the effect of resistive load nonlinearity, future studies may address nonlinear modulation of the load reactance, which can be achieved by filling the gap with a suitable nonlinear Kerr medium.[22,32] We note that the milled antennas were robust against picosecond pumping at a fluence of several mJ/cm^2, as illustrated by comparing SEM images before and after illumination (see Supporting Information). Visible damage occurred using high-intensity infrared radiation around 1060 nm wavelength and at fluences around 100 mJ/cm^2.

In conclusion, using helium ion milling we have successfully fabricated plasmonic nanoantennas loaded with a metallic bridge of various dimensions. By calibrating the helium ion milling process, we could calibrate the amount of vertical milling up to nm precision. This has allowed for the first time to reproducibly fabricate partially loaded antennas with a nanometer-sized metallic bridge in the gap using vertical milling. This geometry is of particular interest because of the greatly improved sensitivity to the bridge dimensions owing to the small thickness of the antenna compared to its width. It is shown that a few-nm thick metal bridge is sufficient to change the nature of the gap loading from capacitive to inductive. Using single-particle spectroscopy, we have accessed the absolute optical cross sections of these antennas in the near-infrared range both in the linear and nonlinear regime. Absolute extinction cross sections were in agreement with numerical models; in particularly the spectra showed a plasmonic Fano resonance between different resonance orders of a single antenna, which was predicted theoretically but not yet reported experimentally. The Fano

profile was shown to appear more clearly when analyzing the nonlinear modulation spectra, which was possible due to our single-particle pump-probe experiments. Single-particle pump-probe spectroscopy showed an increase of the relative nonlinear signal for intermediate bridge dimensions of around 5 nm. This shows that manipulation of the antenna load can be used to enhance the nonlinear antenna response without changing its physical length. Helium ion milling pushes the limits of control over plasmonic nanostructures and opens up new opportunities for achieving new regimes of electron transport. While the results of our current studies could be explained using classical and local theories, further reduction of the nanogaps may open up new areas of nonlocal[2] and quantum plasmonics.[3]

Acknowledgement

This work was supported by EPSRC through grant EP/J011797/1, O.M. acknowledges support through an EPSRC fellowship EP/J016918/1.

Supporting Information Available

Supporting Information with atomic force microscopy, additional spectra of helium ion milled antennas, background information on circuit theory, fano profiles and model for nonlinear response. This material is available free of charge via the Internet at http://pubs.acs.org. This material is available free of charge via the Internet at `http://pubs.acs.org/`.

References

(1) Novotny, L.; van Hulst, N. Nat. Photon **2011**, 5, 83–90.

(2) Wiener, A.; Duan, H.; Bosman, M.; Horsfield, A. P.; Pendry, J. B.; Yang, J. K. W.; Maier, S. A.; Fernández-Domínguez, A. I. ACS Nano **2013**, 7, 6287–6296.

(3) Savage, K. J.; Hawkeye, M. M.; Esteban, R.; Borisov, A. G.; Aizpurua, J.; Baumberg, J. J. Nature **2012**, 491, 574–577.

(4) Scholl, J. A.; García-Etxarri, A.; Koh, A. L.; Dionne, J. A. Nano Letters **2013**, 13, 564–569.

(5) Duan, H.; Fernández-Domínguez, A. I.; Bosman, M.; Maier, S. A.; Yang, J. K. W. Nano Letters **2012**, 12, 1683–1689.

(6) Wu, Y.; Hong, W.; Akiyama, T.; Gautsch, S.; Kolivoska, V.; Wandlowski, T.; de Rooij, N. F. Nanotechnology **2013**, 24, 235302.

(7) Neubrech, F.; Weber, D.; Katzmann, J.; Huck, C.; Toma, A.; Di Fabrizio, E.; Pucci, A.; Hartling, T. ACS Nano **2012**, 6, 7326–7332.

(8) Schnell, M.; García-Etxarri, A.; Huber, A. J.; Crozier, K.; Aizpurua, J.; Hillenbrand, R. Nat. Photon. **2009**, 3, 1749–4885.

(9) Alber, I.; Sigle, W.; Demming-Janssen, F.; Neumann, R.; Trautmann, C.; van Aken, P. A.; Toimil-Molares, M. E. ACS Nano **2012**, 6, 9711–9717.

(10) Postek, M. T.; Vladar, A. E.; Kramar, J.; Stern, L. A.; Notte, J.; McVey, S. AIP Conference Proceedings **2007**, 931, 161–167.

(11) Winston, D.; Cord, B. M.; Ming, B.; Bell, D. C.; DiNatale, W. F.; Stern, L. A.; Vladar, A. E.; Postek, M. T.; Mondol, M. K.; Yang, J. K. W.; Berggren, K. K. J. Vac. Sci Technol. B **2009**, 27, 2702–2706.

(12) Marshall, M. M.; Yang, J.; Hall, A. R. Scanning **2012**, 34, 101–106.

(13) Lemme, M. C.; Bell, D. C.; Williams, J. R.; Stern, L. A.; Baugher, B. W. H.; Jarillo-Herrero, P.; Marcus, C. M. ACS Nano **2009**, 3, 2674–2676, PMID: 19769403.

(14) Wang, Y.; Boden, S. A.; Bagnall, D. M.; Rutt, H. N.; de Groot, C. H. Nanotechnology **2012**, 23, 395302.

(15) Melli, M.; Polyakov, A.; Gargas, D.; Huynh, C.; Scipioni, L.; Bao, W.; Ogletree, D. F.; Schuck, P. J.; Cabrini, S.; Weber-Bargioni, A. Nano Letters **2013**, 13, 2687–2691.

(16) Unal, N.; Charlton, M. D.; Wang, Y.; Waizmann, U.; Reindl, T.; Hofmann, U. Microelectronic Engineering **2011**, 88, 2158 – 2162.

(17) Zeigler, J. F.; Biersack, J. P.; Littmark, U.; Reindl, T. The Stopping and Range of Ions in Solids; 2012.

(18) Wang, Y.; de Groot, C. H.; Claudio-González, D.; Charlton, M. D. B. Proc. SPIE **2011**, 8100, 81000P.

(19) Arbouet, A.; Christofilos, D.; Del Fatti, N.; Vallée, F.; Huntzinger, J. R.; Arnaud, P., L.and Billaud; Broyer, M. Phys. Rev. Lett. **2004**, 93, 127401.

(20) Muskens, O. L.; Billaud, P.; Broyer, M.; Del Fatti, N.; F., V. Phys. Rev. B **2008**, 78, 205410.

(21) Husnik, M.; Klein, M. W.; Feth, N.; Kñig, M.; Niegemann, J.; Busch, K.; Linden, S.; Wegener, M. Nat. Photon. **2008**, 2, 614–617.

(22) Abb, M.; Albella, P.; Aizpurua, J.; Muskens, O. L. Nano Lett. **2011**, 11, 2457–2463.

(23) Abb, M.; Wang, Y.; Albella, P.; de Groot, C. H.; Aizpurua, J.; Muskens, O. L. ACS Nano **2012**, 6, 6462–6470.

(24) Liu, N.; Wen, F.; Zhao, Y.; Wang, Y.; Nordlander, P.; Halas, N. J.; Alú, A. Nano Letters **2013**, 13, 142–147.

(25) López-Tejeira, F.; Paniagua-Domínguez, R.; R., R.-O.; Sánchez-Gil, J. A. New J. Phys. **2012**, 14, 023035.

(26) López-Tejeira, F.; Paniagua-Domínguez, R.; Sánchez-Gil, J. A. ACS Nano **2012**, 6, 8989–8996.

(27) Balanis, C. A. Antenna Theory; John Wiley & Sons, 2005.

(28) Novotny, L. Phys. Rev. Lett. **2007**, 98, 266802.

(29) Alù, A.; Engheta, N. Nat. Photon. **2008**, 2, 307–310.

(30) Wang, Y.; Li, Z.; Zhao, K.; Sobhani, A.; Zhu, X.; A., F.; Halas, N. J. Nanoscale **2013**, ASAP.

(31) Baida, H.; Mongin, D.; Christofilos, D.; Bachelier, G.; Crut, A.; Maioli, P.; Del Fatti, N.; Vallée, F. Phys. Rev. Lett. **2011**, 107, 057402.

(32) Chen, P. Y.; Argyropoulos, C.; Alù, A. Nanophotonics **2012**, 1, 221–233.

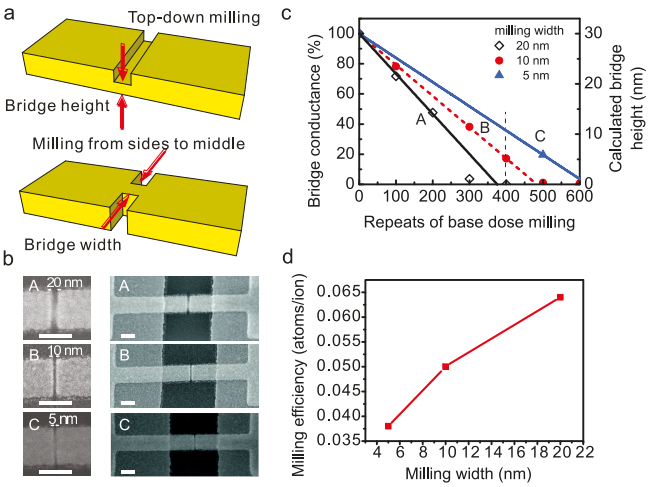

Figure 1: (a) 3-D schematic diagram of milling from the top and milling from sides to middle. (b) SEM images of 30 nm thick Au wires milled by helium ion beam with milling pattern widths of 20 nm, 10 nm and 5 nm. Scale bar, 100 nm. (c) Plot of calculated bridge height of helium ion beam milling area according to the 4-point I-V measurement result. The height of the bridge is considered to be proportional to the conductance. The thin film resistivity increase caused by the interface scattering and non-perfection of the film has been considered. (d) Plot of milling efficiency against pattern width of the milling.

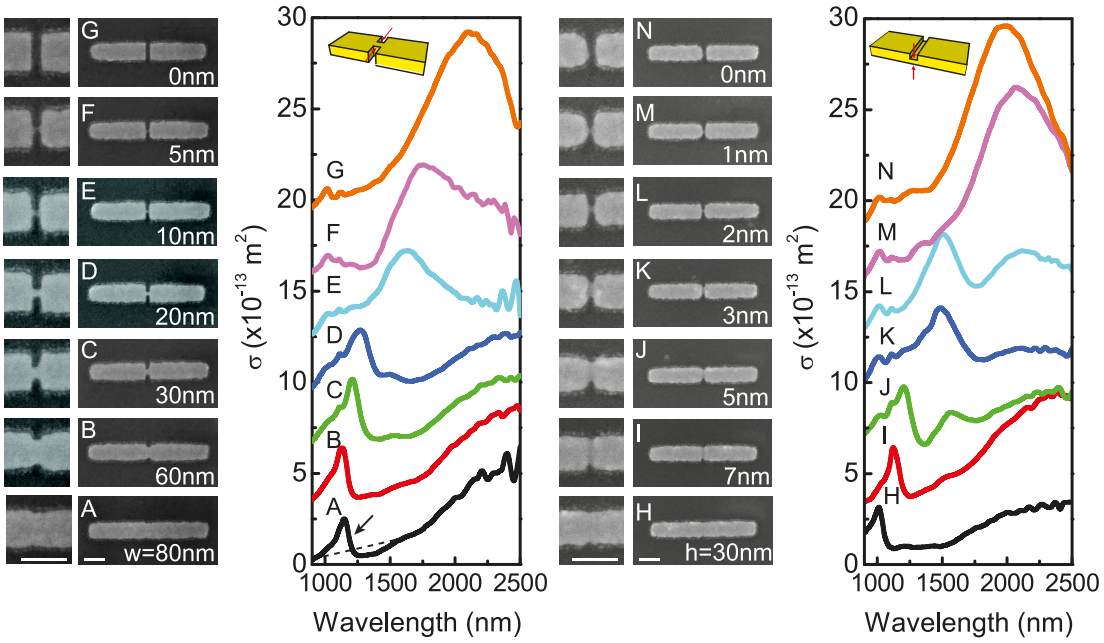

Figure 2: SEM images and single-particle optical spectra of two series of nanoantennas after helium ion beam milling from the sides (**A**-**G**) and from the top (**H**-**N**). Both series were done with 400 repeats of base dose, with a milling width of 20 nm for the side-milled antennas. For milling from the top, the milling width was increased from 5 nm to 20 nm. SEM images are shown for each nanoantenna with a detailed inset of the milled nano-gaps, scale bars 100 nm. Absolute optical extinction cross-sections σ of the corresponding antennas were obtained using Spatial Modulation Microscopy, for longitudinal polarization. Arrow in A indicates single-antenna Fano resonance according to Ref.[26]

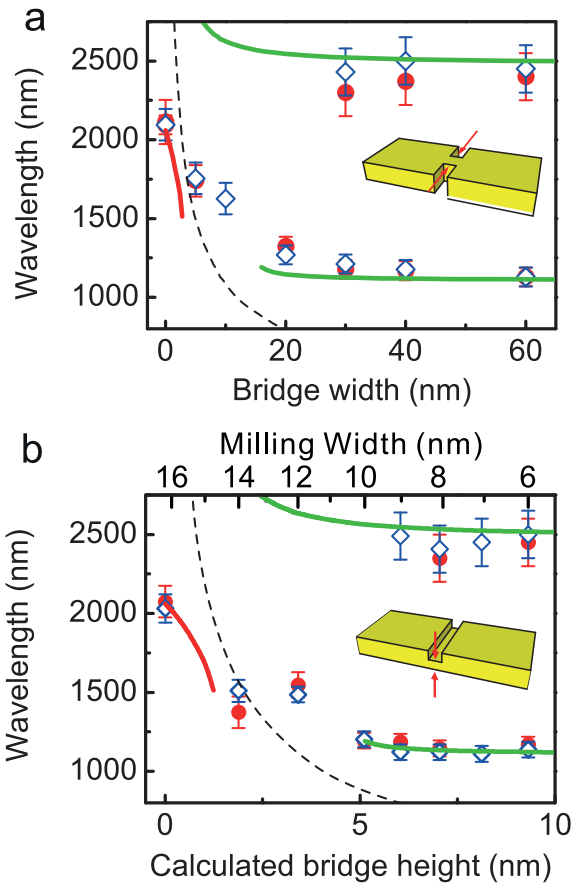

Figure 3: Measured resonance wavelengths for series corresponding to changes in bridge width (a) and height (b). Data taken from spectra of Figure 2 (diamonds, blue) and Supplementary Information (dots, red). Lines correspond to circuit theory, with bonding (thick lines) and antibonding antenna resonances (thin lines) and critical transition from capacitive to inductive load reactance (dashed line).

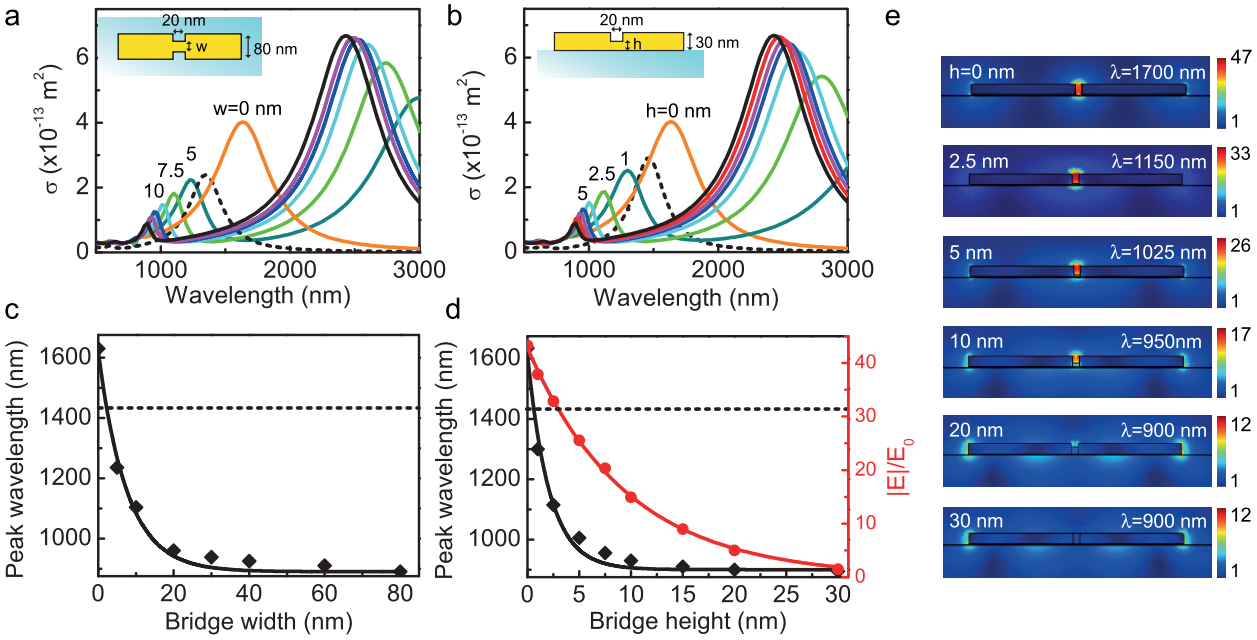

Figure 4: (a,b) Calculated spectra as function of the width (at constant height of 30 nm, a) and height (at constant width of 80 nm, b) of the conducting Au-bridge. (c) Resonance wavelengths versus bridge width from a. (d) Same for bridge height from b (diamonds) with calculated maximum near-field enhancement in the middle of the nanogap (red dots). Dashed lines in a-d, resonances for single arm antenna, corresponding to zero coupling. (e) Calculated near-field distributions at the resonance frequency showing the transition from a $3\lambda/2$ mode at $h = 30$ nm to $\lambda/2$ resonances over each individual arm at $h = 0$ nm.

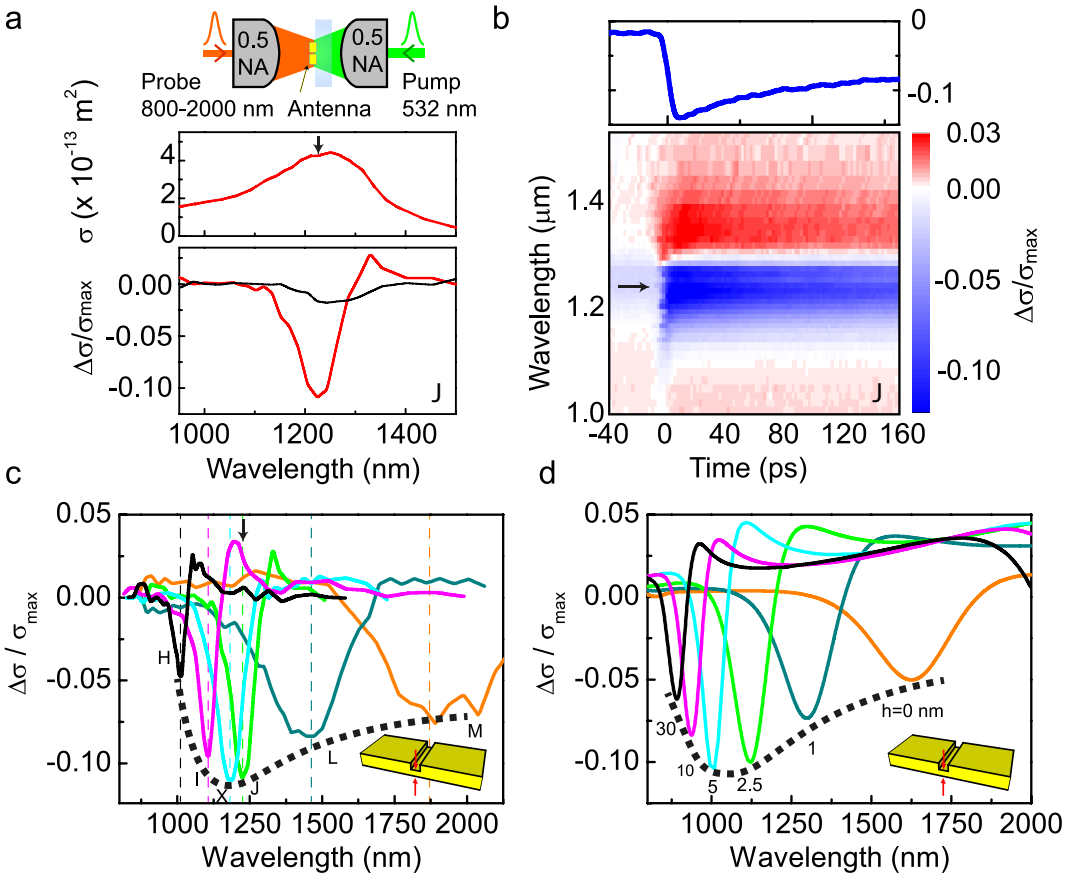

Figure 5: (a) Experimental configuration (top) with measured linear (σ) and nonlinear ($\Delta\sigma/\sigma_{\max}$) response of antenna J, with $\sigma_{\max}$ the cross section at the resonance. Red line, ultrafast response after thermal background correction, black line thermal background. (b) Dynamics of nonlinear antenna response with time trace at 1230 nm. (c) Experimental nonlinear pump-probe signals $\Delta\sigma/\sigma_{\max}$, for different milled antennas. Vertical dashed lines indicate corresponding antenna resonance positions (see Supporting Information). (d) Calculations of nonlinear signal for the antennas of Figure 4b, using nonlinear coefficients from Drude model with nonlinear change in damping time τ_D (see Supplementary Information). Thick dashed lines, guide to the eye indicating optimum in nonlinear response for partially milled antennas.